Check for updates

Nanoengineered Pt–V catalysts promote efficient methanol oxidation in carbon nanotubes†

Muhammed Bekmezci, [ID] [ac] Hasan Donat Yildizay,*[b] Busra Kokoglu[ab] and Fatih Sen [ID] *[a]

In parallel with the developments in the field of energy, research on fuel cells, a renewable energy source, has accelerated. At this rate, the catalysts developed for fuel cells are of great importance. In this study, Platinum (Pt) and Vanadium (V) nanomachines supported on Multi-Walled Carbon Nanotubes (MWCNT) were successfully synthesized by the chemical reduction method, as it is a fast method. Alkaline medium was preferred as the buffer solution for the catalysts used in the methanol oxidation reaction (MOR). The morphology, particle size, and composition of the synthesized PtV@MWCNT catalysts were analyzed by Transmission Electron Microscopy (TEM), Scanning Electron Microscope (SEM), Raman Spectroscopy, and X-ray Diffractometer (XRD). The particle size of the PtV@MWCNT structure was measured as 4.40 nm and the crystallite size as 1.49 nm according to the Debye–Scherer equation. The MWCNT-supported bimetallic nanocatalysts showed 40.72% higher electrochemical activities compared to the monometallic V catalyst at ambient temperature, with MOR activity higher than that of the Pt structure. The catalytic activity of the PtV@MWCNT nanostructure was times higher than that of the PtV structure. Finally, the high catalytic activity, increased durability, and improved stability of PtV@MWCNT make this catalyst emerge as a promising electrocatalyst for the development of direct alcohol fuel cells. This study yielded innovative results demonstrating the activity of metal V-based bimetallic catalysts in the catalysts required for MOR. The research is highly valuable for fuel cell applications.

1. Introduction

Energy is an important element of development for the world economy.[1] Creating a global sustainable energy system to protect our environment is one of the most important challenges facing humanity. With the onset of the Industrial Age, carbon dioxide (CO_2) emissions have increased significantly to the present day. While the CO_2 rate in the atmosphere was 278 ppm in the 1750 s, it increased by 50% to 417 ppm by 2022.[2] This is generally due to energy production methods. Accordingly, it also brings with it significant environmental problems.[3–5] Therefore, the production and consumption of energy have emerged as significant global concerns.[6] For this reason, alternative energy sources have become more remarkable than before, as pollution caused by fossil fuels causes an energy crisis.[7,8] Despite the increase in global electrical energy demand, the production of fossil fuels is expected to decrease

significantly by 2050 due to the shift towards renewable energy.[9] As we go toward renewable energy, nanostructures are becoming increasingly significant.[10] While wind energy, solar energy, and hydroelectricity are important branches of renewable energy, each still has significant constraints.[11] In addition, fuel cells are an important solution to the energy crisis surrounding the world.[12] Fuel cells are one of the renewable clean energies of the future. Among renewable energy sources, fuel cells are recognized as a promising energy source with advantages such as high specific energy density, low cost, and high operating efficiency.[7,8] Having an electrochemical method, the fuel cell is a power conversion device that converts chemical energy into electrical energy by oxidation of a fuel (at the anode) and a corresponding reduction of oxygen gas (at the cathode).[13,14] There are a variety of fuel cells available, the most common being solid oxide fuel cells (SOFC), molten carbonate fuel cells (MCFC), and proton exchange membrane fuel cells (PEMFC).[15] Another important type is direct methanol fuel cells (DMFCs). This fuel cell is a type of clean energy conversion device that provides a solution to environmental concerns worldwide.[16]

Transition metal nanoparticles are frequently used to improve the catalytic properties of fuel cells.[17] Among these metals, the one that attracts the most attention is platinum (Pt).[18] Platinum is a structurally ideal catalyst for the methanol

[a]*Sen Research Group, Department of Biochemistry, Dumlupinar University, Kutahya, Turkey. E-mail: fatihsen1980gmail.com*
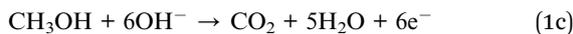
[b]*Department of Mechanical Engineering, Faculty of Engineering, Dumlupinar University, Kutahya, Türkiye. E-mail: hasan.yildizay@dpu.edu.tr*

[c]*Department of Materials Science & Engineering, Faculty of Engineering, Dumlupinar University, Kutahya, Turkey*

oxidation reaction (MOR).[19] Also, diverse free-standing and supported ternary Pt-based catalysts exhibiting distinct morphologies (*e.g.*, nanodendrites, nanowires, and nanocubes) and compositions (*e.g.*, alloy, core–shell, and intermetallic) have been developed for the methanol oxidation reaction (MOR). The morphology and composition influence the MOR activity.[20] Understanding the interaction between alcohols and metal electrocatalysts is crucial for MOR. Formaldehyde, formic acid and carbon dioxide are the primary products produced during the methanol oxidation reaction.[21] A high H_2 production rate in electrolysis can be achieved through the complete oxidation of methanol to CO_2. This is because a greater number of electrons ($6e^-$) are involved for the complete reaction compared to the other products ($2e^-$ and $4e^-$, respectively). The reaction kinetics are shown in eqn (1). As indicated by MOR, the catalyst is also very important. Research into reducing the cost of Pt will allow the development of cost-effective fuel cell systems.[22–24]

$$CH_3OH + 2OH^- \rightarrow CH_2O + 2H_2O + 2e^- \quad (1a)$$

$$CH_3OH + 4OH^- \rightarrow HCOOH + 3H_2O + 4e^- \quad (1b)$$

$$CH_3OH + 6OH^- \rightarrow CO_2 + 5H_2O + 6e^- \quad (1c)$$

Carbon supports such as carbon black, graphite nanofibers, and carbon nanotubes (CNT) are often incorporated into the Pt structure.[25] The use of carbon (C)-based nanostructures is also particularly valuable in electrochemistry.[26,27] However, its use as a C derivative, multi-walled carbon nanotube (MWCNT), has generated great interest in fuel cell applications.[28] These materials are as cost-reducing and energy-transfer efficient as polymers, ceramics, or other carbon derivatives. It has properties such as high conductivity, specific surface area, porosity, and good dispersion. MWCNT, the best catalyst support material compared to many others, has better corrosion resistance.[29] MWCNTs show a high electrocatalytic activity and a high resistance to CO poisoning.[30] As a result of all these properties, MWCNT has increased its use as an excellent electrode support for fuel cells due to its stability in alkaline and acidic media.[31] For example, one study synthesized PtPdCu nanodendrite (PND) structures and found them to exhibit a dense array of branches, open corners, interconnected pores, and high surface area. The methanol oxidation reaction (MOR) mass activity of PtPdCu PNDs (3.66 mA per μgPt) was reported to be 1.45, 2.73, and 2.83 times higher than that of PtPd PNDs, PtCu PNDs, and commercial Pt/C, respectively, based on the equivalent Pt mass. The study highlighted the formation of a structure resistant to CO poisoning.[32]

At the same time, from a chemical point of view, the main method to overcome the problems such as low electrocatalytic activity in electrochemical is the use of bimetallic catalysts.[33] Alloying Pt with cheaper transition metals such as nickel, cobalt, copper, and iron has created not only lower Pt content but also higher methanol oxidation activity.[11,19] At the same time, cathode catalysts such as Pt–Ni or Pt–Co are among the bimetallic catalysts used in fuel cells.[35] The metal (Ni or Co) dissolves and leaches from the surface layer into the acid electrode, leaving behind a Pt top layer.[36] Vanadium (V) can also be

considered a metal that has a good synergy with Pt. Vanadium oxide nanotubes (VO$_x$-NTs) are of particular interest because of their morphology with four different contact sites and many functionalities.[37] Compared to carbon nanotubes (CNTs), VO$_x$-NTs are more easily accessible to pure products at low temperature and have much higher reactive activity due to the abundant defects on their surface.[38] Extensive work is being done in areas such as VO$_x$, gas sensing, and catalysis. Their variable electronic structure and chemical reducibility are remarkable.[39] It has a significant effect on electrical conductivity and catalytic activity. In recent years, significant progress has been made on these species.[40]

In DMFC technology, it can lead to poisoning of active sites caused by toxic CO-like intermediates adsorbed on the catalyst surface.[41] These shortcomings significantly hinder the commercialization of DMFC technology.[10,16] Instead of Pt, catalysts made of more widely available, cheap elements can be used. But, due to the acidic and oxidizing environment of PEMFC, few thermodynamically stable elements are available. Although the activities of these elements are close to or better than Pt, its generally exhibit lower electroactive properties due to their low resistivity or low active site density.[42] Due to such factors, instead of replacing Pt, it is aimed to improve Pt activity or to support it with different metal groups.[43] Accordingly, V with bond energies of about 500 kJ mol^{-1}, respectively, was preferred as the second element to be added to Pt to investigate the activity of the catalysts during the methanol oxidation process.[44] Also, the interplay between the catalyst and the support material is a crucial determinant influencing the efficacy of the oxygen reduction reaction (ORR). The interactions established between the Pt nanoparticles and the MWCNT support surface, which includes V, provide dynamic interfaces akin to Pt–OH–H$_2$O–V@MWCNT. This structure modulates the binding of reaction intermediates and enhances ORR kinetics by promoting proton transport. Consequently, the support material functions both as a carrier and as an integral component of the active interface.[45]

This study investigates the effects of V metal on the catalytic activity of PtV@MWCNT in the oxidation of methanol. Therefore, Pt, V, and PtV structures were also studied separately. The electrocatalytic properties of the synthesized nano catalysts were investigated by cyclic voltammetry (CV). The phase morphology, composition, and structural properties of the prepared catalysts were investigated. Important findings were obtained in terms of both affordable cost and high stability of the catalyst obtained. This study has revealed very important results in terms of demonstrating the usability of V metal in different catalyst applications and gaining more place in the application.

2. Materials & methods

2.1. Materials

Platinum tetrachloride (PtCl$_4$), vanadium(III) chloride (VCl$_4$), sodium borohydride (NaBH$_4$), multiwalled Carbon nanotube (MWCNT), dimethylformamide (DMF-99%), and L-ascorbic acid (99%) were obtained from Sigma-Aldrich and Nafion D-521 Alfa

Aesar. All purchased chemicals were of high purity and were used without any purification process.

2.2. Synthesis of Pt, PtV, and PtV@MWCNT nanostructure

As the first step, the synthesis phase was started with the chemical reduction method. The synthesis was carried out according to the literature. Briefly;[34] Pt–V/MWCNT nanocomposite was synthesized *via* chemical reduction using sodium borohydride (NaBH$_4$) as a reducing agent in the presence of multi-walled carbon nanotubes (MWCNTs) as a support matrix. In a typical synthesis, stoichiometric amounts of 10 mM PtCl$_4$ and 10 mM VCl$_4$ were diluted in deionized water. Then, MWCNTs were added to the metal precursor solution under nitrogen atmosphere. A well-cooled unit was installed in the Schlenk system. The cooling water inlet temperature was 20 °C. It was anticipated that the rapid reduction ability of NaBH$_4$ would facilitate the immediate nucleation and deposition of metallic Pt^{4+} and V^{4+}/V^5 species on the MWCNT surfaces. NaBH$_4$ was added to the system at a concentration of 0.1 M. Stirring was continued for 2 hours to ensure sufficient adsorption of the Pt^{4+} and V^{4+}/V^{5+} species onto the nanotube surfaces. The reaction mixture turned from yellow-brown to black, indicating that the reduction was successful. Stirring was continued for another 2 hours at room temperature to complete the reaction. The mixture was then sonicated in a sonication bath for 30 min to reduce agglomeration. After this process, the mixture was centrifuged at 5000 rpm. The process was also washed 3 times with dH$_2$O to remove unwanted compounds in the medium. It was dried at ambient temperature for 24 hours. The synthesis and characterization stages are expressed in Scheme 1.

2.3. Electrochemical characterization

A potentiostat/galvanostat was used for electrochemical analysis in the study (Gamry Reference 3000). A standard three-electrode system was used for electrochemical experiments. Platinum plate counter electrode, Ag/AgCl reference electrode, and glassy carbon (GCE) working electrode constitute this electrode system. Before electrochemical experiments, the working electrodes were subjected to ultrasonication for 30 min. Then, the GCE surface was polished with 0.1 μm, 0.5 μm and 1 μm slurry of alumina and washed with 70% methanol and then with distilled water. This process was applied to the GCE surface before each experiment. At the same time, the ohmic resistance of the working electrode was measured using a manual multimeter. For each GCE optimization, the modification method was applied by drop casting (10 μL). Before each application, the mixture was vortexed to eliminate precipitation. A modification solution was prepared for this modification process. Briefly,[46] 10 mg NP powder, 500 μL dH$_2$O, 37.5 μL Nafion D-521, and 75 μL DMF were added to the modification solution and then sonicated for 30 minutes. After this, the prepared three-electrode system was used to take measurements for cyclic voltammetry (CV), and impedance (EIS). Measurements were performed in the potential range from −0.8 V to 0.2 V using 1 M KOH solution containing 1 M CH$_3$OH. In addition, to evaluate the activity of the catalyst at different scan rates, it was also evaluated with increasing scan rate (SR) by electrochemical measurement method. Measurements were carried out at scan rates of 50 mV s^{-1}, 100 mV s^{-1}, 150 mV s^{-1}, 200 mV s^{-1} and 250 mV s^{-1} in 1 M KOH solution containing 1 M CH$_3$OH.

2.4. Material structure characterization

The Transmission Electron Microscope (TEM – JEOL 1220 JEM) was operates 120 kW with a tungsten electron source and aperture size 50×–20 000×, X-ray diffraction (XRD – Rigaku Miniflex), Scanning Electron Microscope (SEM – QUANTA 400F), and Raman Spectrometry (Raman – Renishaw inVia) lasers: 532 nm, 735 nm devices were used to characterize the obtained nanostructures.

3. Results & discussion

3.1. Material characterization

The nanostructure obtained was characterized through TEM analysis. The concentrations of Platinum (Pt), Vanadium (V), and platinum–vanadium@multiwalled carbon nanotube (PtV@MWCNT) were determined separately. As demonstrated in Fig. 1, TEM clearly shows all three structures. The Pt NPs structures obtained were spherical and approximately 7.91 nm in size.[47] The uniformly distributed structures were generally far from the agglomerate. The rod form was observed in the V NPs structure because of chemical reduction and temperature adjustment. The V rods had a diameter of 3.59 nm.[48] V-rods can be said to have partial agglomered zones.[48] A different structure was observed in the forms produced using MWCNT, with a particle size of 4.40 nm. Likewise, the synthesis involving MWCNT revealed the existence of tubular structures. The transmission electron microscopy (TEM) data reveals that the distribution of Pt and V nanoparticles on the surface of multiwalled carbon nanotubes (MWCNTs) is partially even. The particles attached to the surface of MWCNTs are nearly spherical, enabling the estimation of their average size. The presence of partial Agromere in certain regions is believed to be a result
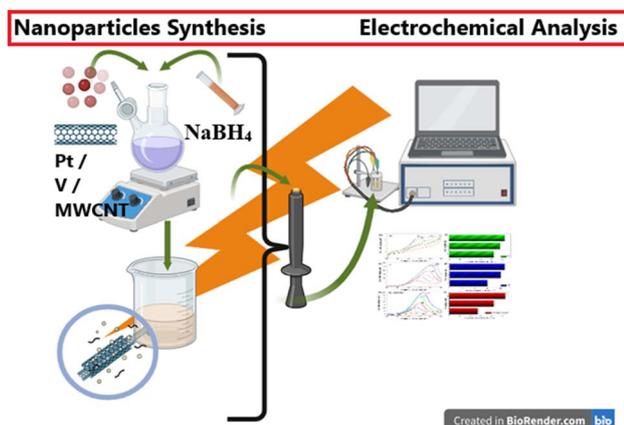
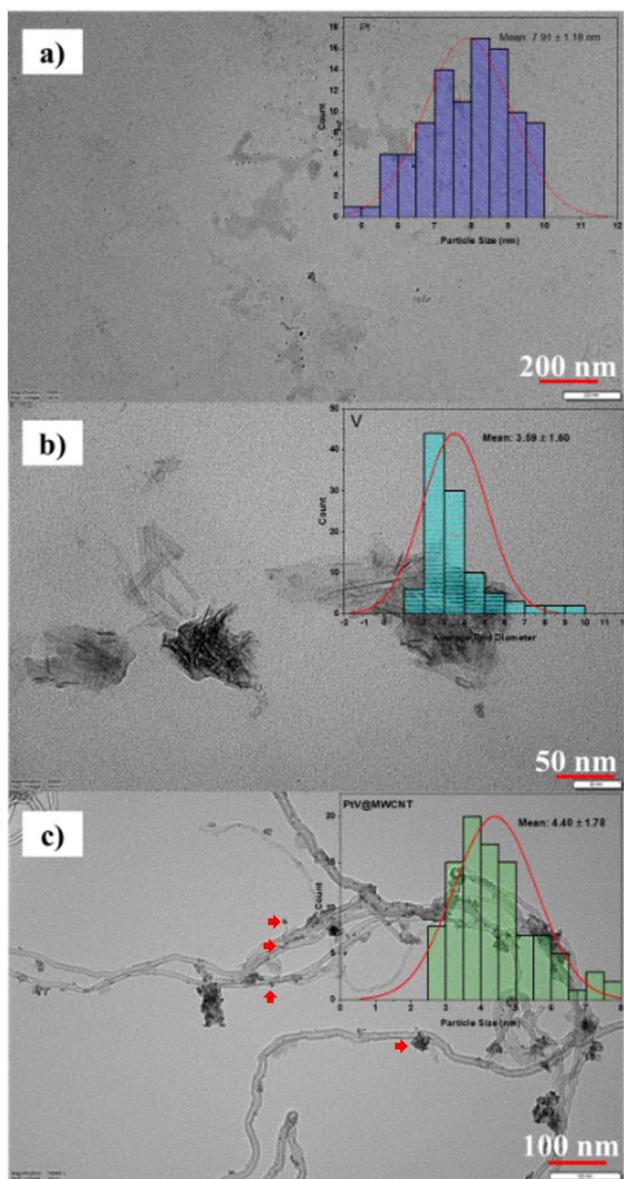Scheme 1 Nanoparticles synthesis and characterization stage.

Fig. 1 TEM images and particle distribution histogram graphs of particles obtained by chemical reduction method, (a) Pt NPs, (b) V NPs, (c) PtV@MWCNT NPs.

of temperature regulation during synthesis.[49] The synthesis stage, a crucial step in the study, was conducted in accordance with the literature, as evidenced by the TEM graph. XRD was employed as the second method of material characterization in the study.

The D and G bands observed in the spectrum of carbon nanotubes in Raman spectroscopy provide important information about the structural properties and chemical interactions of the material. The D band is located in the 1300–1350 cm^{-1} range and is associated with defects or distortions in the structure of carbon nanotubes. This band reflects deviations of sp^2 carbon atoms from the regular graphite structure, surface defects, edge effects, or interactions with heteroatoms. A higher D band intensity indicates an increase in the defect rate of the sample.

The G band is located in the 1500–1600 cm^{-1} range and represents the ordered graphite structure of sp^2-hybridized carbon atoms. This band defines the regular hexagonal lattice and crystal structure of carbon nanotubes. Shifts in the position or intensity of the G band indicate a change in the chemical environment or bonding state of the material. Interactions with metal atoms or the formation of hybrid bonds can lead to shifts in the energy of this band. In the PtV@MWCNT compound, the observed positions and intensity ratios (I_D/I_G) of the D and G bands reveal the structural properties of carbon nanotubes and the degree of interaction with metal atoms. V and Pt can affect the graphite structure by forming chemical bonds with the surface of the nanotubes. These interactions lead to an increase in the intensity of the D band, while shifts or intensity changes can be observed in the G band. Such shifts are due to effects such as the disruption of sp^2 carbon structures or the direct binding of metal atoms to carbon atoms. It can be seen that the D band shows a degree of imperfection (I_D/I_G) that provides the diffraction of the D band to the G band. A higher humidity indicates increased defects of the carbon nanotubes, while a lower humidity is indicative of a more ordered and crystalline structure. V and Pt products have been observed to increase these distributions, which allows the metal atoms to connect to the nanotubes and form defective circuits. But the degree of the shift in the G band can provide more information about the connectivity of these communications and the type of connection. In particular, a shift of the G band to lower energy indicates the presence of hybrid bonds or surface adsorption. The Raman spectrum of images containing V and Pt reflects the structural and electronic design as well as the chemical interactions between the two materials. Although Pt is a Raman-active metal, certain changes in the spectrum can be observed as a result of its interaction with V. These changes are usually distinguished from the formation of metallic or hybrid bonds between the surface of V and Pt atoms. It suggests that the interaction of Pt with V causes shifts in the Raman modes or the appearance of new selection modes, thereby changing the chemical binding environment of vanadium. In particular, it has been observed in the graphical Raman spectrum of vanadium in the oxidation state, leading to the formation of new peaks or changes in the position and intensity of existing peaks. These changes can be attributed to the catalytic effect of Pt atoms on the chemical state modulus of V. During the spectral analysis, shifts or new modes and changes in peak widths are notable, indicating interactions between V and Pt. The broadening of the peaks may indicate that Pt atoms disrupt the regularity of the V structure, forming a more amorphous structure. In addition, the increase in the intensity of certain Raman-active modes indicates that Pt atoms have formed a binding site on the V surface. The effect of Pt on the vibrational modes of V is clearly visible in the spectrum obtained. Pt has been shown to cause a rearrangement of energy levels in the Raman spectrum of V by changing the electron transfer and surface charge density. This effect is particularly pronounced in cases of hybrid bond formation or surface adsorption. The structural effects of such interactions can be evaluated in more
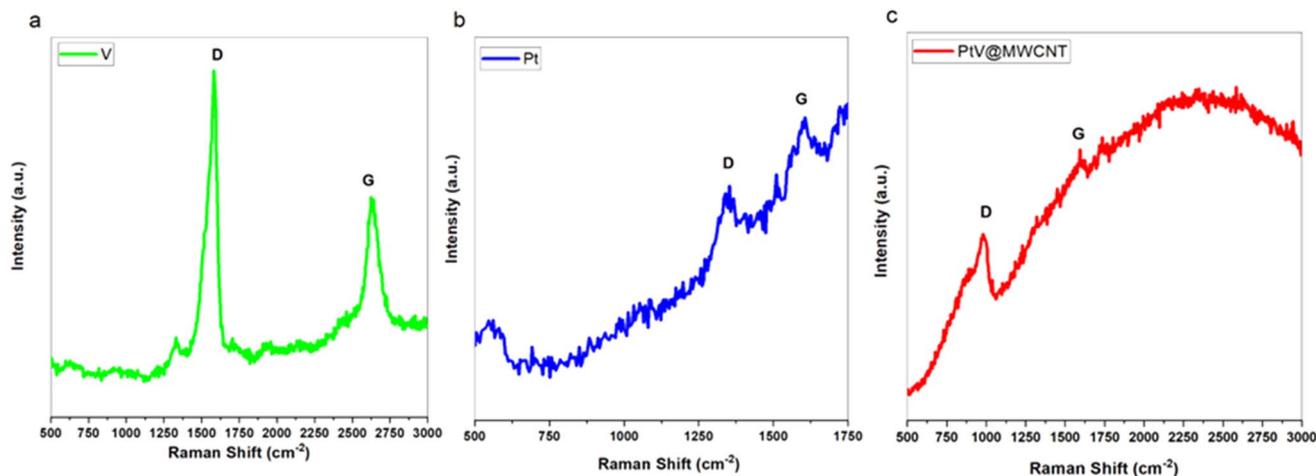
Fig. 2 Raman analysis results for the nanocatalysts synthesized. (a) V, (b) Pt, and (c) PtV@MWCNT.

detail by comparative spectral analysis with other materials. Fig. 2 shows the Raman spectra for V, Pt, and PtV@MWCNT.

SEM analysis was performed as a further analysis. The surface of the V sample is irregular, and the particles are clearly separated. The particles have sharp edges and a micro-scale structure, indicating that the crystal structure of V is highly ordered but brittle. There are cracks and rough areas on the surface, indicating that the mechanical strength of the material may be limited, but may be advantageous in terms of active surface area in certain applications. However, the catalytic performance of this structure may be limited by how reactive the surface is and the size of the particles. Looking at the Pt–V example, we can see that a more dense and homogeneous structure forms on the surface due to the way V and Pt interact. The Pt atoms are on the surface of the vanadium and cause it to change its shape, creating a more amorphous structure. This means that the surface area can grow and the catalytic properties of the material can improve. Pt atoms also adhere to the crystal structure of V, making the surface rougher, which can be interpreted as making the surface more reactive, especially when used as a catalyst in gaseous or liquid environments. The PtV@MWCNT sample shows a very different surface structure due to the carbon nanotubes. The multi-walled carbon nanotubes form a binding network structure between the V and Pt particles, creating a dense, porous texture on the surface. This structure increases the mechanical strength and significantly increases the active surface area of the sample. The porous and bonded structure of the material allows it to interact more effectively with liquid or gaseous media, and the carbon nanotubes help the material to remain structurally sound over time. The structural differences between these three examples are quite striking when it comes to surface morphology and material interactions that directly affect the performance of the materials. Pt, when added to the basic V structure, makes the surface denser, and we think it will help carbon nanotubes develop properties that will allow the material to better resist both chemicals and electricity. This structure has the potential to be used in all kinds of fields, including energy storage,

catalysis, and sensor technologies. Fig. 3 shows SEM analysis of the synthesized particles. Also, EDX analyses are shown in Fig. S1.† In the analysis, the regions of the V, Pt and Pt, V, and C structures were marked and found to be consistent with the SEM images.

XRD was performed as another analysis. The morphological properties of the structure obtained for the PtV@MWCNT structure yielded significant results when compared with TEM. The XRD analysis confirmed the diffractive indices of Pt and V noble metals supported by MWCNT. The XRD pattern of the produced PtV@MWCNT nanocomposite was examined to determine the crystallographic structure and the average crystallite size of the metallic phase. Prominent diffraction peaks indicating the face-centered cubic (FCC) structure of Pt were evident.[50] However, the combination of V and Pt led to significant changes in the diffraction peaks associated with Pt. A small shift to the right in the 2θ values was observed, which was interpreted as lattice expansion induced by the addition of V atoms to the Pt lattice.[51] This phenomenon was interpreted as arising from the difference in atomic radii between Pt and V, where partial substitution or alloying effects deform the crystal lattice, changing the interplanar spacing as explained by Bragg's law.[52] It was shown that the full width at half maximum (FWHM) of the Pt (111) and (200) peaks increased after V integration.[53] The broadening of diffraction peaks indicates a decrease in crystallite size, which was also confirmed quantitatively using the Debye–Scherrer equation.[54] This significant particle size reduction can be attributed to the inhibitory effect of V on Pt particle growth during synthesis, as V can alter the nucleation and growth dynamics of Pt NPs, leading to more dispersed and finer crystallites.[55] Furthermore, peak broadening and lattice distortion suggest that a solid solution or alloy formation may have occurred between Pt and V, rather than a purely physical association.[56] This alloying tendency alters the crystallographic properties and is interpreted to also affect the electronic structure of Pt, which is necessary for MOR catalytic activity.[57] The reduced crystallite size and potential lattice strain further increase the surface energy, increasing the number of
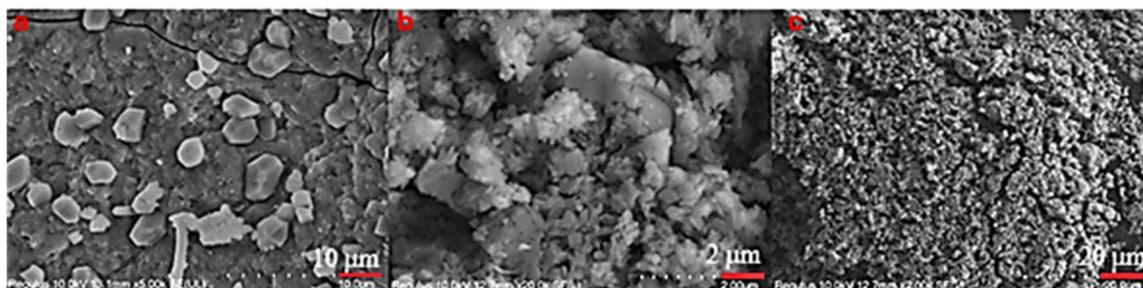
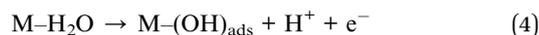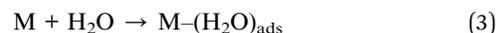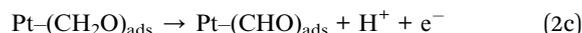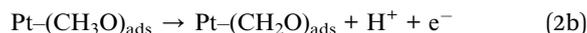Fig. 3 SEM images of (a) V NPs, (b) Pt NPs, and (c) PtV@MWCNT NPs.

accessible active sites.[58] Structural analysis using XRD shows that the addition of V significantly reduces Pt crystallite size while altering the lattice properties and peak profiles.[59] These properties are expected to significantly impact the electrocatalytic activity of the nanocomposite, particularly in terms of bulk activity and long-term stability.[60]

Fig. 4 shows that the integrated structure of Pt and V nanoparticles was successfully obtained with MWCNT. The lattice parameters for Pt(111), Pt(200), and Pt(220) are 40.11°, 46.29°, and 67.95°, respectively. At the same time, partial contractions can be observed due to V. For V, the parameters correspond to the Pt indices according to Vegard's law, and the intensity values increase. In addition, the MWCNT-induced C(000) parameter was approximately 2θ at 25°. The analysis results indicate compliance with reference code 03-065-1527.[29,30] Also, in XRD analysis of the PtV@MWCNT nanocomposite, the crystallite size was calculated to be approximately 1.49 nm using the Debye–Scherrer equation. This value indicates that the material has very small, nanoscopic crystallites.[61,62] Such low crystallite sizes are generally associated with high surface area, increased number of active centers, and a significant improvement in catalytic performance.[63] Especially in catalytic applications of precious metals such as Pt, these small particle sizes lead to an increase in the electrochemical active surface area

(ECSA) due to the greater number of surface atoms compared to larger atoms.[64] This provides higher mass activity and specific activity, particularly in electrochemical energy conversion systems such as fuel cells and in applications such as MOR.[65] Furthermore, the use of Pt with V can be interpreted as both increasing the stability of the crystal structure and creating a synergistic effect by altering the electronic structure.[66] These modifications can be considered to increase tolerance to CO poisoning and improve the rate of reactions such as MOR by affecting the electron density of Pt centers.[67] The MWCNT carrier facilitates the homogeneous distribution of these nanoparticles, while also increasing electrical conductivity and supporting mechanical strength.[68]

3.2. Electrochemical characterization

Following material characterization, electrochemical analysis was conducted. As is well known, Pt is a highly stable metal with excellent electrocatalytic activity. For this reason, it is commonly used in electrochemical sensor applications and fuel cells.[25,31–33] However, the high cost of Pt restricts its development in fuel cell technologies.[69–71] Ley *et al.* have demonstrated the mechanism of methanol oxidation in acidic media, which is a potential mechanism for Pt, to proceed according to the following equation.[72]

$$Pt–(CH_3OH)_{ads} \rightarrow Pt–(CH_3O)_{ads} + H^+ + e^- \quad (2a)$$

$$Pt–(CH_3O)_{ads} \rightarrow Pt–(CH_2O)_{ads} + H^+ + e^- \quad (2b)$$

$$Pt–(CH_2O)_{ads} \rightarrow Pt–(CHO)_{ads} + H^+ + e^- \quad (2c)$$

$$Pt–(CHO)_{ads} \rightarrow Pt–(CO)_{ads} + H^+ + e^- \quad (2d)$$

$$M + H_2O \rightarrow M–(H_2O)_{ads} \quad (3)$$

$$M–H_2O \rightarrow M–(OH)_{ads} + H^+ + e^- \quad (4)$$

$$Pt–(CO)_{ads} + M–(OH)_{ads} \rightarrow Pt + M + CO_2 + H^+ + e^- \quad (5)$$

They showed that M affects the rates of reactions (3)–(5) directly and the rates of reactions (1) and (2a) indirectly through electronic changes in Pt. M represents the component/particle, constituent or promoter metal. In fact, the efficiency of the M–Pt catalyst is reflected in the strength of the M–O bond, which depends on both the dehydrogenation of the absorbed water
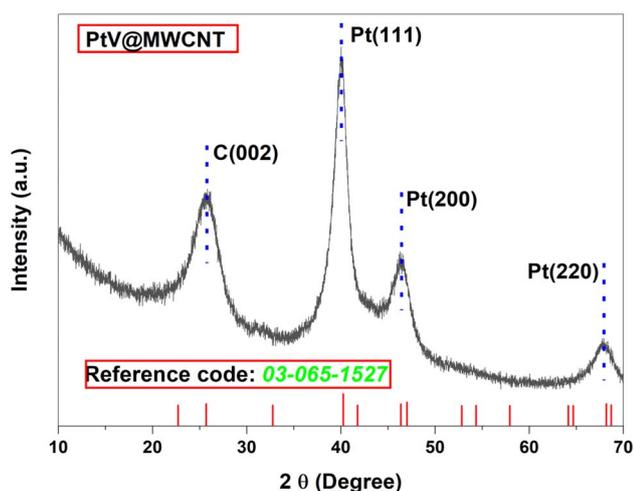

Fig. 4 XRD patterns and reference code of PtV@MWCNT nanostructure obtained by chemical reduction method.
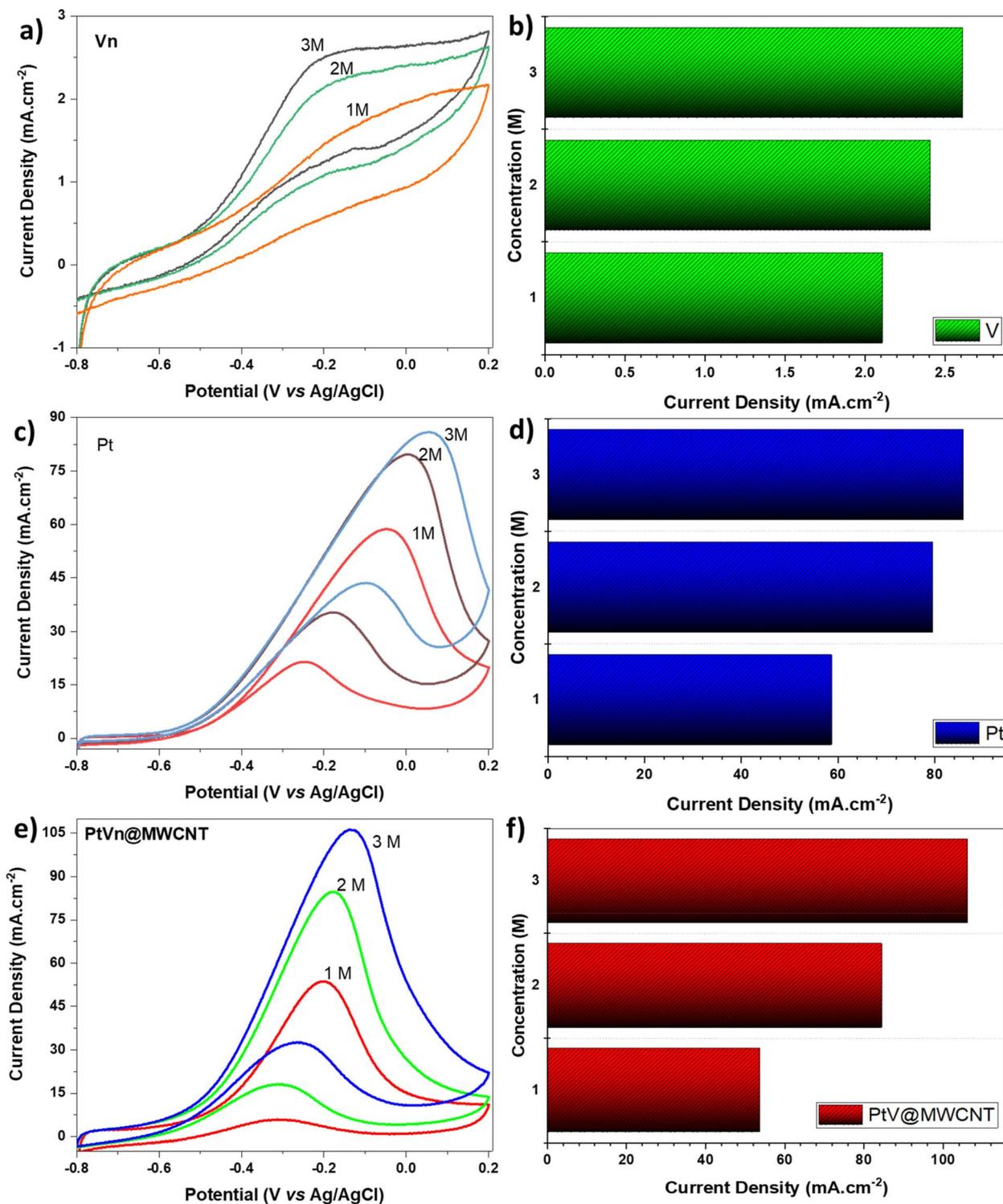
Fig. 5 CV for V, Pt, and PtV@MWCNT nanocatalysts obtained by chemical reduction method, obtained at different methanol ratios (0.5 M KOH, 50 mV s^{-1}), (a) CV obtained for V catalyst, (b) positive current values obtained for V catalyst (c) CV obtained for PT catalyst, (d) positive current values obtained for Pt catalyst, (e) CV obtained for PtV@MWCNT catalyst, (f) positive current values obtained for the PtV@MWCNT catalyst.

(reactions (3) and (4)) and the ability to cleave the M–O bond to form CO_2 (reaction (5)).

In view of all this, the methanol oxidation reactions to be obtained were analyzed separately for Pt, V and PtV@MWCNT

by cyclic voltammetry (CV), and electrochemical impedance (EIS). As a first analysis, a CV study was performed and the rates of change in current with increasing methanol ratios were examined. To determine the electrochemical activity of the

synthesized catalysts, CV measurements with V, Pt and PtV@MWCNT were evaluated between −0.8 and 0.2 V at 50 mV s^{-1} in 0.5 M potassium hydroxide (KOH) solution saturated with nitrogen gas (N$_2$). As shown in Fig. 5a–e, the three catalysts exhibit characteristic CV behavior of Pt-based materials in alkaline medium, particularly with irreversible anodic peaks associated with the MOR. At lower potentials, the suppression of adsorption/desorption currents is likely due to the poisoning effect of CO-like intermediates formed during methanol adsorption on the catalyst surface, which block active sites and hinder further oxidation. In the high-potential region, broad oxidative currents correspond to the formation and reduction of Pt oxides, which regenerate active surface sites for further methanol oxidation. The poisoning rate is highest for the V catalyst or is due to the low electrocatalytic activity of V. However, poisoning of the Pt surface can also result from the dehydrogenation of carbonaceous intermediates by methanol on Pt. Moreover, the initial oxidation potential and the peak current density in the anodic potential sweep are one of the main parameters to evaluate the electrocatalytic performance of catalysts. During the positive current (I_p) potential scan, the methanol oxidation current gradually increases in all three catalysts until it starts around −0.6 V. Meanwhile, the lowest value of the positive current potential onset can be said to belong to the PtV@MWCNT catalyst. Similarly, it is evident that partially semi-reversible reactions occur for V, while reversible reactions occur for Pt and Pt@MWCNT structures. The reverse negative sweep (I_n) indicates a potential of approximately −0.2 V. The I_n scan peak values correspond to the oxidation of carbonaceous intermediates formed during the anodic scan. Furthermore, the I_p/I_n ratio can serve as an indicator of the toxicity of the reaction medium. Accordingly, the I_p/I_n ratios for V, Pt, and PtV@MWCNT catalysts in a 3 M methanol medium were determined to be 1.85, 1.98, and 3.26, respectively. As can be seen, PtV@MWCNT catalyst has the highest rate and it can be said that the toxicity is also the lowest. This can be attributed to MWCNT and V catalyst.[73]

As previously stated, one effective method for determining catalyst poisoning is to calculate the ratio of positive and reverse current values. Table 1 presents the I_n, I_p, and I_p/I_n ratios. At this point, the current values obtained with the PtV@MWCNT structure can be given as the ideal ratio.

That being said, it is also very important to compare the positive current values obtained at different methanol ratios with each other. Fig. 6 displays the graph of current values obtained for V, Pt, and PtV@MWCNT structures. The graph indicates that Pt-containing catalysts exhibit high catalytic activity. As can be seen from the CV, it can be said that these current values give a very good reversible reaction. However, it is evident that in 1 M methanol fuel medium, the performance of the PtV@MWCNT catalyst is inferior to that of the Pt catalyst. This may be attributed to electrode defects in the GCE or to media stabilization. Additionally, the current catalyst values obtained with Pt and Pt@MWCNT structures are comparable to or higher than those reported in the literature. In the 3 M methanol medium, the PtV@MWCNT catalyst achieved

Table 1 The current values for both positive (I_p) and negative (I_n) and the I_p/I_n ratios for V, Pt, and PtV@MWCNT catalysts obtained through chemical synthesis are presented

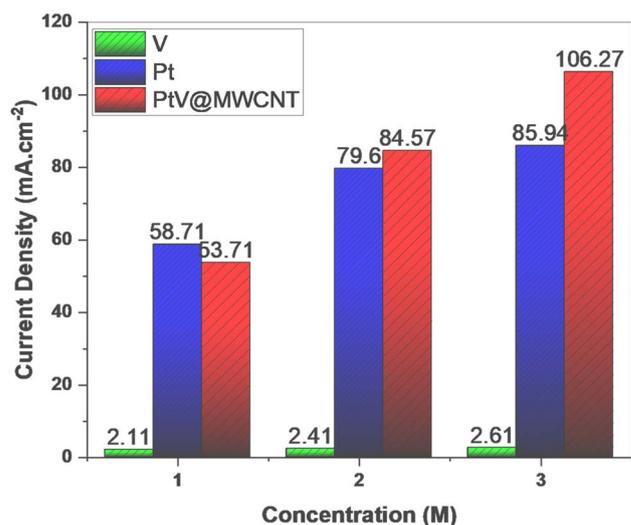| Catalysis	V (mA cm^{-2})	Pt (mA cm^{-2})	PtV@MWCNT (mA cm^{-2})
I_n	1.41	43.51	32.57
I_p	2.61	85.94	106.27
I_p/I_n	1.85	1.98	3.26

Fig. 6 A comparison was made of the positive current values obtained for V, Pt, and PtV@MWCNT nanocatalysts synthesized by the chemical reduction method.

a 40.72% higher current value than the V catalyst and a 1.24% higher current value than the Pt catalyst.

The obtained CV values have made significant contributions to literature regarding the current values required when using V as a catalyst. In addition, the current values obtained at different scan rates for V, PT, and PtV@MWCNT catalysts also gave us results to gain insight into catalyst poisoning and fuel transport to the catalyst. Fig. 7a, c and d compares the values obtained for all three catalysts at 50 mV s^{-1}, 100 mV s^{-1}, 150 mV s^{-1}, 200 mV s^{-1}, and 250 mV s^{-1} at 1 M methanol content. The correlation between the square roots of scanning speeds and the current values obtained at those speeds was analyzed. Additionally, the potential scan rate used can determine the size of the diffusion layer above the electrode surface. In general, the diffusion layer will form continuously. With a low potential scan rate, it will tend to grow above the electrode. In this case, the bulk will result in less concentration gradient between the solution and the electrode surface. In this case, the target compound is expected to result in a lower mass flux. As a result, the magnitude of the electrochemical current, which is proportional to the mass transport rate of methanol towards the electrode, will grow larger with an increase in the potential scan rate. For the V nanostructures utilized in the study, the current limit values indicate that the electrochemical kinetic rate at the
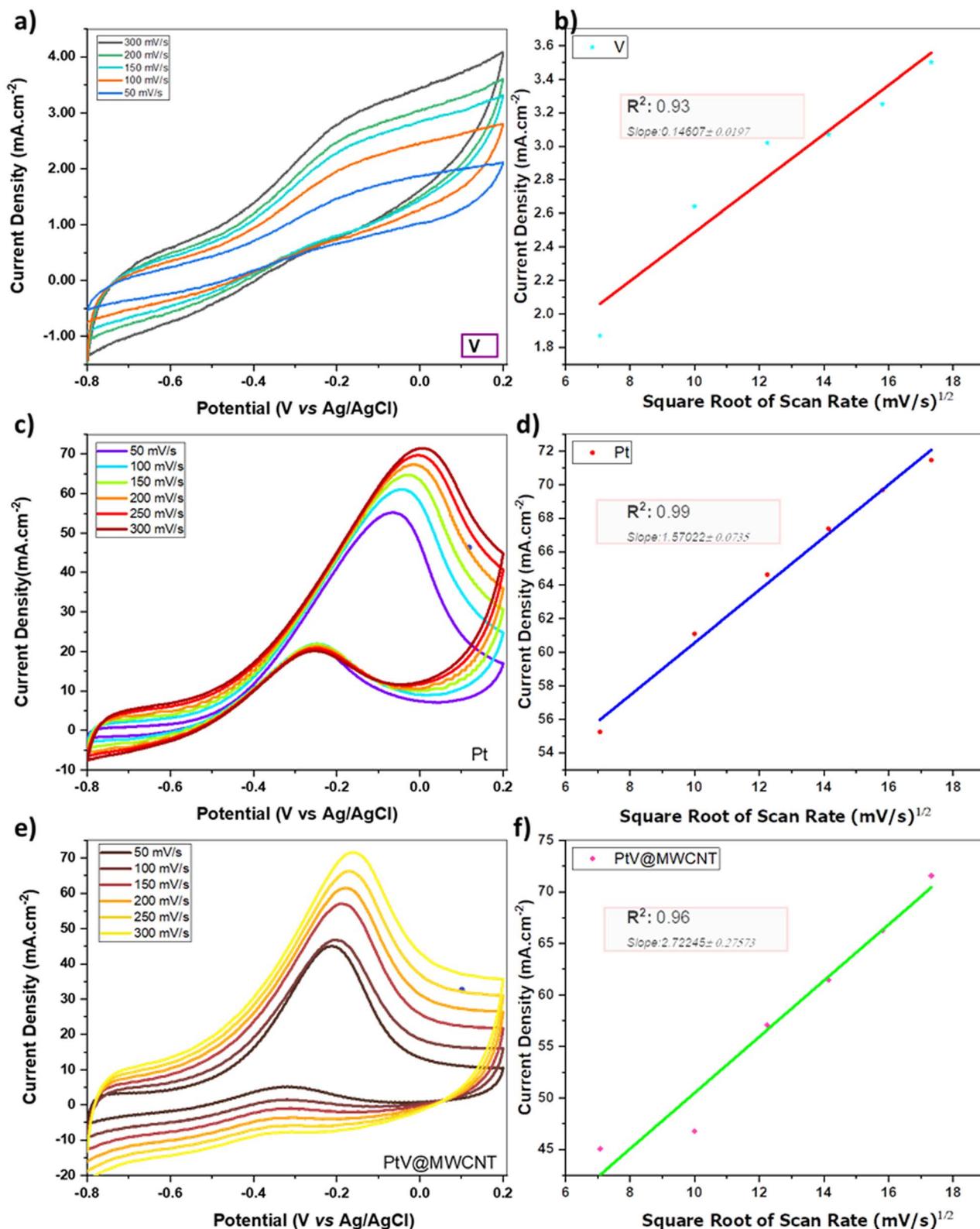
Fig. 7 Current values of 50 mV s^{-1}, 100 mV s^{-1}, 150 mV s^{-1}, 200 mV s^{-1}, 250 mV s^{-1}, 250 mV s^{-1}, realized in 1 M methanol content and, 0.5 M KOH buffer for nanoparticles produced by chemical synthesis, (a) CV curves obtained for V nanoparticle, (b) correlation of the square root of the scan rate for the V nanoparticle with the current obtained, (c) CV curves obtained for Pt nanoparticle, (d) correlation between the square root of the scan rate and the current obtained for the Pt nanoparticle, (e) CV curves obtained for PtV@MWCNT nanoparticles, (f) correlation of the square root of the scan rate with the current obtained for PtV@MWCNT nanoparticles.

electrode is insufficient to reach equilibrium at the solution–electrode interface. Although the structure obtained with Pt Np was the most ideal, the PtV@MWCNT structure exhibited current values that were very similar to those of Pt. At the same time, the final limit current value is slightly better than the structure obtained with the Pt catalyst. Thus, it was anticipated that the resulting catalyst could function as a bimetallic nanostructure equivalent to Pt. Fig. 7b, d and f demonstrate a linear correlation between the square root of the scan rate and the positive boundary current in the current values obtained. Based on this correlation, it appears that the reaction occurs in a diffusion-controlled manner for all three catalysts. At the same time, the partial rightward shift of the Pt nanostructure is an indication that its tolerance to ambient poisoning is gradually decreasing. In the PtV@MWCNT structure, this shift was very limited compared to the Pt nanostructure.[32,36–38] Additionally, the CV method was used to calculate the electrochemical active surface area (ECSA).[74–76] ECSA represents the surface area of an electrode material capable of participating in electrochemical reactions and is a critical parameter for evaluating the material's effectiveness, particularly in fuel cells, supercapacitors, and electrocatalysis applications.[77] C_{dl} represents the capacitance of the electrical double layer formed between the electrode surface and the electrolyte and is related only to the capacitive currents generated by the physical adsorption of ions onto the electrode surface.[78] Therefore, this region, where chemical redox reactions do not occur, is called the "non-faradic region." For this study, the CV curves obtained at different scan rates were considered.[79] For each scan rate, the anodic and cathodic current values were taken, and the absolute value of the difference between these two values was divided by two. As a result of this process, the capacitive current observed in the non-faradic potential region was calculated.[80] ECSA was calculated by comparing this value with the specific capacitance C_s for the material (Pt, V, PtV@MWCNT) obtained from literature. These results indicate that the surface areas of all three samples are different, and that the carbon nanotube-supported PtV@MWCNT alloy, in particular, offers a higher active surface area compared to other materials. This demonstrates the advantage of this structure for electrochemical applications and the surface area enhancement capacity of nanostructured support materials.[81] According to this method, the ECSA values for V, Pt, and PtV@MWCNT were found to be 0.00017 cm^2, 0.00094 cm^2, and 0.00104 cm^2, respectively. Therefore, ECSA calculation based on the capacitive current method can be considered an effective method, particularly for material comparisons and surface engineering studies.[82] A long-term stability analysis was also performed in Fig. S2.† This analysis was performed to monitor the appropriate behavior in the whole-cell analysis. The current values obtained in the analysis increased with increasing cycle rates. Although a partial shift was observed, it can be concluded that the toxicity was limited.

The V catalyst-coated electrode failed to reach a significant value in impedance due to insufficient active surface area or slow reaction kinetics, resulting in high charge transfer resistance and higher energy requirement for the electrochemical

reaction to take place. In contrast, the Pt electrode shows lower impedance, indicating enhanced electron transfer and improved reaction kinetics. Relative to the Pt catalyst, the PtV@MWCNT catalyst exhibits the lowest impedance. This result is important to emphasize that the carbon nanotube coating increases the surface area, accelerates charge transfer, and provides higher catalytic activity on the electrode surface. The values obtained were consistent with the current values obtained in CV analysis. At the same time, it also exhibited behavior in accordance with the literature. The importance of low impedance lies in its ability to minimize energy losses within the system and increase reaction efficiency, thus guaranteeing optimal electrochemical performance. Additionally, the equivalent circuit model was used to describe the impedance properties at the electrode/electrolyte interface in a three-electrode electrochemical cell; specifically, a system with an anodic catalyst coated on a GCE operating in a strongly alkaline medium such as 1 M KOH. The circuit elements in the diagram can be interpreted in relation to the physical and chemical mechanisms of electroanalytical processes. R_1 (R_s) in the circuit represents the total ohmic resistance of the system, that is, the solution resistance resulting from the ionic conductivity of the electrolyte and the intercell junctions. This resistance is generally low due to the high conductivity of a 1 M KOH solution. However, parameters such as the interelectrode distance and membrane properties can affect R_s. Therefore, the R_s value is an important indicator of the overall conductance of the system. R_2 (R_{ct}), also called the charge transfer resistance, represents the kinetic barrier for faradaic reactions occurring at the electrode surface. This parameter provides direct information about the activity and electrochemical kinetics of the catalyst surface, particularly in anodic processes such as the MOR. A low R_{ct} indicates that electron transfer occurs readily at the catalyst surface and is associated with high electrochemical performance. C_3 (C_{dl}), connected in parallel with the circuit, is modeled as a double-layer capacitance. This capacitance
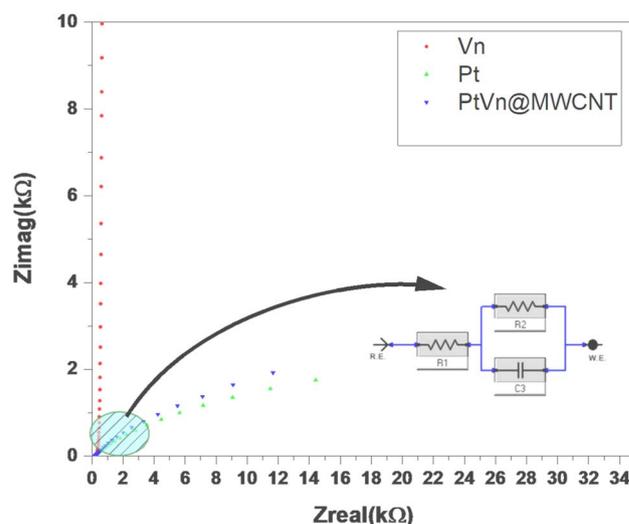

Fig. 8 EIS analysis for synthesized catalysts (0.5 M KOH).

Table 2 Comparative analysis of results from the study and existing literature

Electrocatalysis	Solution	Alcohol	Scan rate mV s^{-1}	Anodic peak current (mA cm^{-2})	References
PtPb	1 M KOH	1 M CH$_3$OH	50 mV s^{-1}	5.7	83
PtPb PNW	0.5 M H$_2$SO$_4$	0.5 M CH$_3$OH	50 mV s^{-1}	70.58 mA cm^{-2}	84
Pt@PdS$_2$-MWCNT	0.5 M H$_2$SO$_4$	1 M CH$_3$OH	50 mV s^{-1}	86.71 mA cm^{-2}	85
Pt$_{0.94}$Ag$_{0.06}$NWE	0.5 M H$_2$SO$_4$	1 M CH$_3$OH	50 mV s^{-1}	46.3 mA cm^{-2}	86
PtRu/C$_{70}$MWCNTs$_{30}$	0.5 M H$_2$SO$_4$	1 M CH$_3$OH	50 mV s^{-1}	92.6 mA cm^{-2}	87
PtCo (1 : 11)/rGO	1 M H$_2$SO$_4$	2 M CH$_3$OH	20 mV s^{-1}	17.26 mA cm^{-2}	88
PtV@MWCNT	1 M KOH	1 M CH$_3$OH	50 mV s^{-1}	106.27 mA cm^{-2}	**This work**

represents the charge storage capacity of the electrical double layer formed at the electrode surface. For smooth and conductive surfaces such as GCE, this parameter can vary depending on the electrode surface area, surface roughness, and contact with the electrolyte. The capacitance value can also be evaluated because of interface phenomena such as adsorption/desorption processes or ionic rearrangement. If the curve converges to a 45° line with decreasing frequency, the addition of Warburg diffusion may be necessary, but this component is not included in this circuit. Equivalent circuit modeling is performed for all catalysts. Fig. 8 shows the results of the EIS analysis.

Table 2 presents a comparative analysis of methanol oxidation studies using various electrocatalysts and compares the findings with the existing literature. Literature studies have shown that PtV@MWCNT exhibits significant electrocatalytic activity. The results are consistent with the literature, indicating that the synthesized catalyst is promising for alcohol fuel cell research.
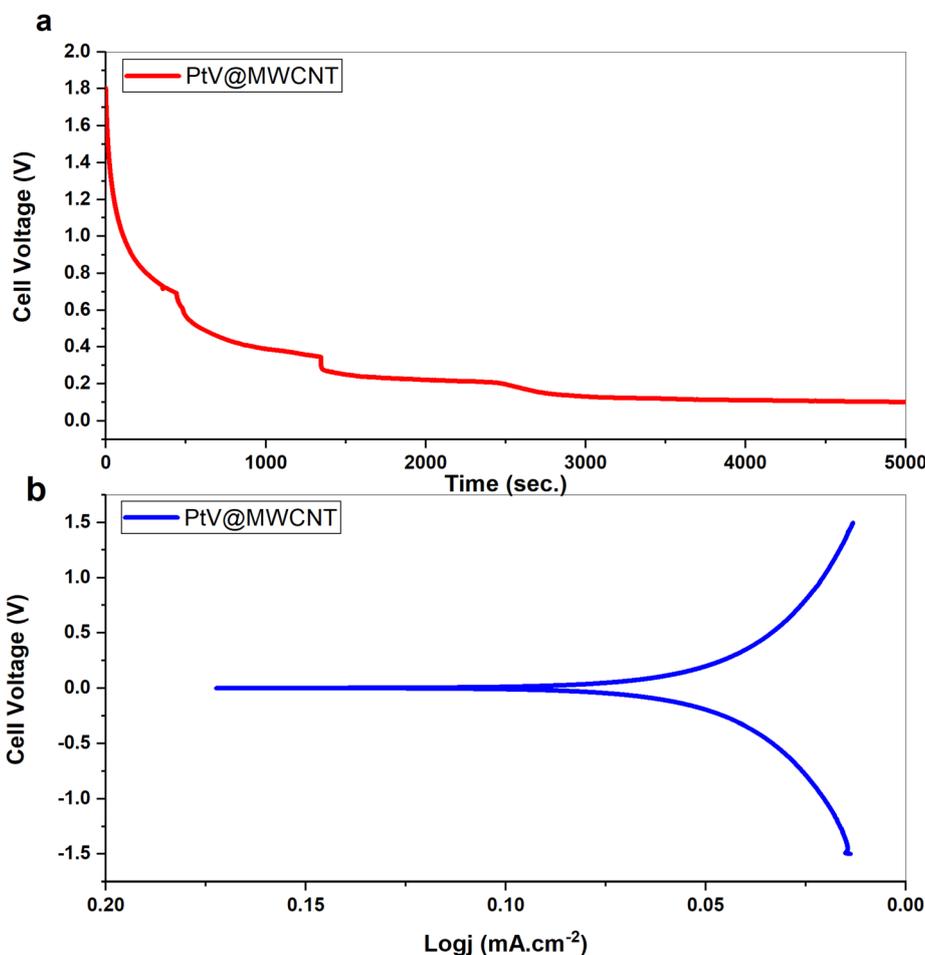

Fig. 9 Potentiostat values obtained for use in thermodynamic analyses for stacked cell in FCs: (a) open current voltage (b) potentiodynamic analysis series.

In the following stages, fuel cell stack studies were performed. In fuel cell stack studies, a two-electrode system was used. The cell was in bulk. Resistance tests were performed for the cell and determined as 1 kΩ. This resistance was used to protect the cell in case of overvoltage and to ensure the stability of the device at positive current values. Fig. 9 shows the open current voltage and potentiodynamic analysis for the full stacked cell. The analysis shows the anodic and cathodic behavior of the cell under maximum voltage and voltage. Distinct Tafel curves were also evaluated for both anode and cathode reactions. This is illustrated by the relationship between the logarithmic current density ($\log j$) and cell voltage (V) on the x-axis and y-axis. The anodic Tafel slope, defined as -120 mV dec^{-1}, was shown to indicate the efficiency of catalytic activity with low overpotential and high reaction kinetics. In contrast, the cathodic slope, defined as 130 mV dec^{-1}, was shown to indicate a higher activation energy. The data obtained from this study confirm that PtV@MWCNT can serve as a high-performance nanocatalyst in fuel cell reactions. It is clear that methanol poisoning still exists in a similar situation. Accordingly, the current value for the fully conditioned cell decreased from 1.8 V to 0.2 V quite rapidly. When the voltage and current values are analyzed, it can be said that the cell never passes into the passive transport phase, and the transport always takes place with active transport. The cell potential onset is around 0 V. This can be interpreted that the catalyst and MEA conditioning are ideal or close to ideal. In addition, it is very good that both anodic and cathodic Tafel curves are close to each other. This can be interpreted as the current generated at the anodic side can be equal to or close to the current passing to the cathode within the specified voltage limit range. In addition, the Butler–Volmer equation was used thermodynamically. Accordingly, $T = 298$ K and Faraday constant: $F = 96\,485$ C mol^{-1}, gas constant: $R = 8.314$ J mol^{-1} and reversible current density, $j_0 = 1 \times 10^{-3}$ A cm^{-2} according to the analysis. When the values were substituted, the charge transfer coefficients $\alpha_a = 0.5$ and $\alpha_c = 0.5$ were found. In addition, according to Darcy's law, the permeability coefficient of the Nafion membrane, $k = 1 \times 10^{-12}$ m^2 and the dynamic viscosity was entered as 0.59 mPa. The pressure difference is assumed to be 1 Pa m^{-1}. The flow velocity (v) $= 1.69 \times 10^{-9}$ m s^{-1} was calculated. These values are the velocities calculated at low permeability and low-pressure difference in a porous medium. Flowing at higher velocities may damage the membrane. The obtained flow rate was quite ideal for the PEM membrane according to the literature.

4. Conclusion

In this research, the PtV@MWCNT composite was effectively formed and used as a catalyst for methanol oxidation processes. According to the electrocatalytic performance tests, the PtV@MWCNT catalyst showed higher activity, higher current density, and improved stability. TEM images confirmed the consistent and stable distribution of PtV on the MWCNT surface, supporting the reported electrochemical performance. The particle size of PtV@MWCNT was analyzed as 4.40 nm. The key factor in the increased catalytic efficiency is the highly conductive network structure formed by the close contact between the nanotubes the matrix, confirming the electrochemical analysis results. According to the MOR result, the PtV@MWCNT catalyst showed outstanding performance, exhibiting high activity and stability. Compared to the V catalyst, a higher electrochemical efficiency of 40.72% was achieved. The improved activity of the catalyst was supported by TEM images, which confirmed the uniform distribution of PtV on the MWCNT surface. These results demonstrate the potential of PtV@MWCNT as a material for future fuel cell applications.

Data availability

Data will be provided if requested.

Conflicts of interest

There are no conflicts to declare.

Acknowledgements

References

1 A. Midilli and I. Dincer, Hydrogen as a renewable and sustainable solution in reducing global fossil fuel consumption, *Int. J. Hydrogen Energy*, 2008, **33**(16), 4209–4222.

2 P. Friedlingstein, M. O'Sullivan, M. W. Jones, R. M. Andrew, D. C. E. Bakker, J. Hauck, *et al.*, Global Carbon Budget 2023, *Earth Syst. Sci. Data*, 2023, **15**(12), 5301–5369.

3 Q. Zeng, C. Li and C. Magazzino, Impact of green energy production for sustainable economic growth and green economic recovery, *Heliyon*, 2024, **10**(17), e36643, available from: **https://linkinghub.elsevier.com/retrieve/pii/S2405844024126746**.

4 M. Bekmezci, D. B. Subasi, R. Bayat, M. Akin, Z. K. Coguplugil and F. Sen, Synthesis of a functionalized carbon supported platinum–iridium nanoparticle catalyst by the rapid chemical reduction method for the anodic reaction of direct methanol fuel cells, *New J. Chem.*, 2022, **46**, 21591–21598, available from: **https://pubs.rsc.org/en/content/articlehtml/2022/nj/d2nj03209k**.

5 R. Bayat, A. El Attar, M. Akin, M. Bekmezci, M. El Rhazi and F. Sen, Copper nanoparticle modified chain-like platinum nanocomposites for electro-oxidation of C1-, C2-, and C3-type alcohols, *Int. J. Hydrogen Energy*, 2024, **51**, 1577–1586.

6 O. Arslan, M. A. Ozgur, H. D. Yildizay and R. Köse, Fuel effects on optimum insulation thickness: An exergitic approach, *Energy Sources, Part A*, 2010, **32**(2), 128–147.

7 Q. Lu, J. Li, K. Eid, X. Gu, Z. Wan, W. Li, *et al.*, Facile one-step aqueous-phase synthesis of porous PtBi nanosponges for

efficient electrochemical methanol oxidation with a high CO tolerance, *J. Electroanal. Chem.*, 2022, **916**, 116361.

8 A. Beheshti, A. K. Marnani, M. B. Askari and A. Hatefi-Mehrjardi, Fe3+-Clinoptilolite/graphene oxide and layered MoS2@Nitrogen doped graphene as novel graphene based nanocomposites for DMFC, *Int. J. Hydrogen Energy*, 2017, **42**(26), 16741–16751.

9 D. Bogdanov, M. Ram, A. Aghahosseini, A. Gulagi, A. S. Oyewo, M. Child, *et al.*, Low-cost renewable electricity as the key driver of the global energy transition towards sustainability, *Energy*, 2021, **227**, 120467.

10 R. Bayat, H. D. Yildizay and F. Şen, Thermopower energy waves propagation in novel generation carbon fibers/fuel composite, *Fuel*, 2025, **385**, 134112, available from: https://linkinghub.elsevier.com/retrieve/pii/S0016236124032630.

11 A. Rahman, O. Farrok and M. M. Haque, Environmental impact of renewable energy source based electrical power plants: Solar, wind, hydroelectric, biomass, geothermal, tidal, ocean, and osmotic, *Renewable Sustainable Energy Rev.*, 2022, **161**, 112279.

12 T. Radhakrishnan and N. Sandhyarani, Three dimensional assembly of electrocatalytic platinum nanostructures on reduced graphene oxide – An electrochemical approach for high performance catalyst for methanol oxidation, *Int. J. Hydrogen Energy*, 2017, **42**(10), 7014–7022.

13 T. Sadhasivam, K. Dhanabalan, S. H. Roh, T. H. Kim, K. W. Park, S. Jung, *et al.*, A comprehensive review on unitized regenerative fuel cells: Crucial challenges and developments, *Int. J. Hydrogen Energy*, 2017, **42**(7), 4415–4433.

14 G. Zhang and S. G. Kandlikar, A critical review of cooling techniques in proton exchange membrane fuel cell stacks, *Int. J. Hydrogen Energy*, 2012, **37**(3), 2412–2429.

15 M. E. Scofield, H. Liu and S. S. Wong, A concise guide to sustainable PEMFCs: recent advances in improving both oxygen reduction catalysts and proton exchange membranes, *Chem. Soc. Rev.*, 2015, **44**(16), 5836–5860, available from: https://pubs.rsc.org/en/content/articlehtml/2015/cs/c5cs00302d.

16 H. Wang, H. Yu, Y. Li, S. Yin, H. Xue, X. Li, *et al.*, Direct synthesis of bimetallic PtCo mesoporous nanospheres as efficient bifunctional electrocatalysts for both oxygen reduction reaction and methanol oxidation reaction, *Nanotechnology*, 2018, **29**(17), 175403, available from: https://iopscience.iop.org/article/10.1088/1361-6528/aaaf3f.

17 M. Bekmezci, D. B. Subasi, R. Bayat, M. Akin, Z. K. Coguplugil and F. Sen, Synthesis of a functionalized carbon supported platinum–iridium nanoparticle catalyst by the rapid chemical reduction method for the anodic reaction of direct methanol fuel cells, *New J. Chem.*, 2022, **46**(45), 21591–21598, available from: https://pubs.rsc.org/en/content/articlehtml/2022/nj/d2nj03209k.

18 X. Ren, Q. Lv, L. Liu, B. Liu, Y. Wang, A. Liu, *et al.*, Current progress of Pt and Pt-based electrocatalysts used for fuel cells, *Sustainable Energy Fuels*, 2019, **4**(1), 15–30, available from: https://pubs.rsc.org/en/content/articlehtml/2020/se/c9se00460b.

19 H. Tian, Y. Yu, Q. Wang, J. Li, P. Rao, R. Li, *et al.*, Recent advances in two-dimensional Pt based electrocatalysts for methanol oxidation reaction, *Int. J. Hydrogen Energy*, 2021, **46**(61), 31202–31215.

20 Q. Lu, X. Zhao, R. Luque and K. Eid, Structure-activity relationship of tri-metallic Pt-based nanocatalysts for methanol oxidation reaction, *Coord. Chem. Rev.*, 2023, **493**, 215280.

21 Y. Liu, R. Wu, Y. Jin, J. Dong, H. Li and J. Wang, Balancing reactant adsorption for ultra-stable electrocatalytic methanol oxidation reaction, *eScience*, 2025, 100430.

22 R. B. Araujo, D. Martín-Yerga, E. C. d. Santos, A. Cornell and L. G. M. Pettersson, Elucidating the role of Ni to enhance the methanol oxidation reaction on Pd electrocatalysts, *Electrochim. Acta*, 2020, **360**, 136954.

23 V. S. Joshi, D. C. Poudyal, A. K. Satpati, K. R. Patil and S. K. Haram, Methanol oxidation reaction on Pt based electrocatalysts modified ultramicroelectrode (UME): Novel electrochemical method for monitoring rate of CO adsorption, *Electrochim. Acta*, 2018, **286**, 287–295.

24 H. Varela, E. A. Paredes-Salazar, F. H. B. Lima and K. Eid, Renewable methanol and the energy challenge: The role of electrocatalysis, *Curr. Opin. Electrochem.*, 2024, **46**, 101539.

25 E. Antolini, Carbon supports for low-temperature fuel cell catalysts, *Appl. Catal., B*, 2009, **88**(1–2), 1–24.

26 G. Zhang, Z. G. Shao, W. Lu, H. Xiao, F. Xie, X. Qin, *et al.*, Aqueous-Phase Synthesis of Sub 10 nm Pd core @Pt shell Nanocatalysts for Oxygen Reduction Reaction Using Amphiphilic Triblock Copolymers as the Reductant and Capping Agent, *J. Phys. Chem. C*, 2013, **117**(26), 13413–13423.

27 Y. Chen, Y. Ma, Y. Zhou, Y. Huang, S. Li, Y. Chen, *et al.*, Enhanced methanol oxidation on PtNi nanoparticles supported on silane-modified reduced graphene oxide, *Int. J. Hydrogen Energy*, 2022, **47**(10), 6638–6649.

28 M. S. Saha and A. Kundu, Functionalizing carbon nanotubes for proton exchange membrane fuel cells electrode, *J. Power Sources*, 2010, **195**(19), 6255–6261.

29 A. Holewinski, J. C. Idrobo and S. Linic, High-performance Ag–Co alloy catalysts for electrochemical oxygen reduction, *Nat. Chem.*, 2014, **6**(9), 828–834, available from: https://www.nature.com/articles/nchem.2032.

30 Z. Cui, P. J. Kulesza, C. M. Li, W. Xing and S. P. Jiang, Pd nanoparticles supported on HPMo-PDDA-MWCNT and their activity for formic acid oxidation reaction of fuel cells, *Int. J. Hydrogen Energy*, 2011, **36**(14), 8508–8517.

31 A. Dector, F. M. Cuevas-Muñiz, M. Guerra-Balcázar, L. A. Godínez, J. Ledesma-García and L. G. Arriaga, Glycerol oxidation in a microfluidic fuel cell using Pd/C and Pd/MWCNT anodes electrodes, *Int. J. Hydrogen Energy*, 2013, **38**(28), 12617–12622.

32 Q. Lu, X. Gu, J. Li, W. Li, R. Luque and K. Eid, Unraveling ultrasonic assisted aqueous-phase one-step synthesis of porous PtPdCu nanodendrites for methanol oxidation with a CO-poisoning tolerance, *Ultrason. Sonochem.*, 2023, **98**, 106494.

33 S. Dongare, N. Singh, H. Bhunia and P. K. Bajpai, Electrochemical reduction of CO2 using oxide based Cu

and Zn bimetallic catalyst, *Electrochim. Acta*, 2021, **392**, 138988.

34 M. Bekmezci, G. N. Gules, R. Bayat and F. Sen, Modification of multi-walled carbon nanotubes with platinum–osmium to develop stable catalysts for direct methanol fuel cells, *Anal. Methods*, 2023, **15**(9), 1223–1229, available from: https://pubs.rsc.org/en/content/articlehtml/2023/ay/d2ay02002e.

35 Y. Sung, J. Hwang and J. S. Chung, Characterization and activity correlations of Pt bimetallic catalysts for low temperature fuel cells, *Int. J. Hydrogen Energy*, 2011, **36**(6), 4007–4014.

36 I. E. L. Stephens, J. Rossmeisl and I. Chorkendorff, Toward sustainable fuel cells, *Science*, 2016, **354**(6318), 1378–1379, available from: https://www.science.org/doi/10.1126/science.aal3303.

37 S. V. Demishev, A. L. Chernobrovkin, V. V. Glushkov, A. V. Grigorieva, E. A. Goodilin, H. Ohta, *et al.*, Magnetic properties of vanadium oxide nanotubes and nanolayers, *Phys. Rev. B:Condens. Matter Mater. Phys.*, 2011, **84**(9), 094426.

38 K. F. Zhang, D. J. Guo, X. Liu, J. Li, H. L. Li and Z. X. Su, Vanadium oxide nanotubes as the support of Pd catalysts for methanol oxidation in alkaline solution, *J. Power Sources*, 2006, **162**(2), 1077–1081.

39 W. C. Vining, A. Goodrow, J. Strunk and A. T. Bell, An experimental and theoretical investigation of the structure and reactivity of bilayered VO/TiO/SiO2 catalysts for methanol oxidation, *J. Catal.*, 2010, **270**(1), 163–171.

40 C. T. Wang, M. T. Chen and D. L. Lai, Surface characterization and reactivity of vanadium–tin oxide nanoparticles, *Appl. Surf. Sci.*, 2011, **257**(11), 5109–5114.

41 W. Mabhulusa, K. E. Sekhosana and X. Fuku, The impact and performance of carbon-supported platinum group metal electrocatalysts for fuel cells, *Int. J. Electrochem. Sci.*, 2024, **19**(4), 100524.

42 S. Hegde, R. Wörner and B. Shabani, Automotive PEM fuel cell catalyst layer degradation mechanisms and characterisation techniques, Part I: Carbon corrosion and binder degradation, *Int. J. Hydrogen Energy*, 2025, **118**, 268–299.

43 I. E. L. Stephens, A. S. Bondarenko, U. Grønbjerg, J. Rossmeisl and I. Chorkendorff, Understanding the electrocatalysis of oxygen reduction on platinum and its alloys, *Energy Environ. Sci.*, 2012, **5**(5), 6744–6762, available from: https://pubs.rsc.org/en/content/articlehtml/2012/ee/c2ee03590a.

44 S. Kianfar, A. N. Golikand and B. ZareNezhad, Bimetallic-metal oxide nanoparticles of Pt-M (M: W, Mo, and V) supported on reduced graphene oxide (rGO): radiolytic synthesis and methanol oxidation electrocatalysis, *J. Nanostruct. Chem.*, 2021, **11**(2), 287–299, available from: https://link.springer.com/article/10.1007/s40097-020-00366-6.

45 J. Zhu, L. Xia, R. Yu, R. Lu, J. Li, R. He, *et al.*, Ultrahigh Stable Methanol Oxidation Enabled by a High Hydroxyl Concentration on Pt Clusters/MXene Interfaces, *J. Am. Chem. Soc.*, 2022, **144**(34), 15529–15538.

46 R. Bayat, A. El Attar, M. Akin, M. Bekmezci, M. El Rhazi and F. Sen, Copper nanoparticle modified chain-like platinum nanocomposites for electro-oxidation of C1-, C2-, and C3-type alcohols, *Int. J. Hydrogen Energy*, 2024, **51**, 1577–1586.

47 A. T. N. Dao, D. M. Mott, K. Higashimine and S. Maenosono, Enhanced Electronic Properties of Pt@Ag Heterostructured Nanoparticles, *Sensors*, 2013, **13**(6), 7813–7826, available from: https://www.mdpi.com/1424-8220/13/6/7813/htm.

48 D. Hu, D. Li, X. Liu, Z. Zhou, J. Tang and Y. Shen, Vanadium-based nanomaterials for cancer diagnosis and treatment, *Biomed. Mater.*, 2020, **16**(1), 014101, available from: https://iopscience.iop.org/article/10.1088/1748-605X/abb523.

49 T. A. B. Santoro, A. O. Neto, R. Chiba, E. S. M. Seo and E. G. Franco, Characterization of Proton Exchange Membrane Fuel Cell Cathode Catalysts Prepared by Alcohol-Reduction Process, *Mater. Sci. Forum*, 2010, **660–661**, 94–99, available from: https://www.scientific.net/MSF.660-661.94.

50 K. J. Chen, K. Chandrasekara Pillai, J. Rick, C. J. Pan, S. H. Wang, C. C. Liu, *et al.*, Bimetallic PtM (M=Pd, Ir) nanoparticle decorated multi-walled carbon nanotube enzyme-free, mediator-less amperometric sensor for H2O2, *Biosens. Bioelectron.*, 2012, **33**(1), 120–127.

51 B. G. Kelly, A. B. Loether, A. D. DiChiara, R. W. Henning, M. F. DeCamp and K. M. Unruh, Lattice parameter evolution in Pt nanoparticles during photo-thermally induced sintering and grain growth, *J. Phys. Chem. Solids*, 2017, **108**, 104–108.

52 C. Xu, C. L. Senaratne, R. J. Culbertson, J. Kouvetakis and J. Menéndez, Deviations from Vegard's law in semiconductor thin films measured with X-ray diffraction and Rutherford backscattering: The Ge1- y Sn y and Ge1- x Si x cases, *J. Appl. Phys.*, 2017, **122**(12), 125702.

53 A. Bahr, T. Glechner, T. Wojcik, A. Kirnbauer, M. Sauer, A. Foelske, *et al.*, Non-reactive HiPIMS deposition of NbCx thin films: Effect of the target power density on structure-mechanical properties, *Surf. Coat. Technol.*, 2022, **444**, 128674.

54 F. Xu, Y. C. Shi and D. Wang, X-ray scattering studies of lignocellulosic biomass: A review, *Carbohydr. Polym.*, 2013, **94**(2), 904–917.

55 L. Wang, A. N. Stuckert, H. Chen and R. T. Yang, Effects of Pt Particle Size on Hydrogen Storage on Pt-Doped Metal−Organic Framework IRMOF-8, *J. Phys. Chem. C*, 2011, **115**(11), 4793–4799.

56 Y. Zhang, Y. J. Zhou, J. P. Lin, G. L. Chen and P. K. Liaw, Solid-Solution Phase Formation Rules for Multi-component Alloys, *Adv. Eng. Mater.*, 2008, **10**(6), 534–538.

57 J. M. Torralba, Improvement of Mechanical and Physical Properties in Powder Metallurgy, in *Comprehensive Materials Processing*, Elsevier, 2014, pp. 281–294.

58 S. Devesa, A. P. Rooney, M. P. Graça, D. Cooper and L. C. Costa, Williamson-hall analysis in estimation of crystallite size and lattice strain in Bi1.34Fe0.66Nb1.34O6.35 prepared by the sol-gel method, *Mater. Sci. Eng., B*, 2021, **263**, 114830.

59 A. H. Diputra, I. K. Hariscandra Dinatha and Y. Yusuf, A comparative X-ray diffraction analysis of Sr2+substituted hydroxyapatite from sand lobster shell waste using various methods, *Heliyon*, 2025, **11**(2), e41781.

60 P. Mohana, S. Swathi, R. Yuvakkumar, G. Ravi, M. Thambidurai and H. D. Nguyen, Co_3O_4/g-C_3N_4 nanocomposite for enriched electrochemical water splitting, *Int. J. Hydrogen Energy*, 2024, **49**, 376–389.

61 A. E. Dwight, J. W. Downey and R. A. Conner, Some AB3 compounds of the transitiom metals, *Acta Crystallogr.*, 1961, **14**(1), 75–76, available from: **https://scripts.iucr.org/cgi-bin/paper?a02989**.

62 J. M. Zhang, S. N. Sun, Y. Li, X. J. Zhang, P. Y. Zhang and Y. J. Fan, A strategy in deep eutectic solvents for carbon nanotube-supported PtCo nanocatalysts with enhanced performance toward methanol electrooxidation, *Int. J. Hydrogen Energy*, 2017, **42**(43), 26744–26751.

63 A. B. D. Nandiyanto, R. Zaen and R. Oktiani, Correlation between crystallite size and photocatalytic performance of micrometer-sized monoclinic WO3 particles, *Arabian J. Chem.*, 2020, **13**(1), 1283–1296.

64 M. Ďurovič, J. Hnát and K. Bouzek, Electrocatalysts for the hydrogen evolution reaction in alkaline and neutral media. A comparative review, *J. Power Sources*, 2021, **493**, 229708.

65 Y. Dessie, E. Tilahun and T. H. Wondimu, Functionalized carbon electrocatalysts in energy conversion and storage applications: A review, *Heliyon*, 2024, **10**(20), e39395.

66 Y. Ma, D. Kang, Y. Wen, Y. Chen, Y. Long, H. Yi, *et al.*, Synergistic effects of Pt single atomic site and Cu nanoclusters for catalytic oxidation of methyl mercaptan, *Appl. Surf. Sci.*, 2024, **657**, 159718.

67 X. Qi, N. Ye, R. Zhang, Z. Jiang and T. Fang, Boosting the activity and CO tolerance for methanol oxidation reaction in alkaline media by constructing the Pt-TMNs electrocatalysts, *Fuel*, 2023, **350**, 128773.

68 E. W. Fenta and B. A. Mebratie, Advancements in carbon nanotube-polymer composites: Enhancing properties and applications through advanced manufacturing techniques, *Heliyon*, 2024, **10**(16), e36490.

69 M. Akin, R. Bayat, V. Erduran, M. Bekmezci, I. Isik and F. Şen, Carbon-based nanomaterials for alcohol fuel cells, *Nanomaterials for Direct Alcohol Fuel Cells: Characterization, Design, and Electrocatalysis*, 2021, pp. 319–336.

70 Z. K. Coguplugil, M. Akin, R. Bayat, M. Bekmezci, H. Karimi-Maleh, A. Javadi, *et al.*, Synthesis and characterization of Pt/ZnO@SWCNT/Fe3O4 as a powerful catalyst for anodic part of direct methanol fuel cell reaction, *Int. J. Hydrogen Energy*, 2023, **48**(55), 21285–21293.

71 M. Akin, M. Bekmezci, R. Bayat, I. Isik and F. Sen, Ultralight covalent organic frame graphene aerogels modified platinum-magnetite nanostructure for direct methanol fuel cell, *Fuel*, 2024, **357**, 129771.

72 K. L. Ley, R. Liu, C. Pu, Q. Fan, N. Leyarovska, C. Segre, *et al.*, Methanol Oxidation on Single-Phase Pt-Ru-Os Ternary Alloys, *J. Electrochem. Soc.*, 1997, **144**(5), 1543–1548, available from: **https://iopscience.iop.org/article/10.1149/1.1837638**.

73 J. J. Fan, Y. J. Fan, R. X. Wang, S. Xiang, H. G. Tang and S. G. Sun, A novel strategy for the synthesis of sulfur-doped carbon nanotubes as a highly efficient Pt catalyst support toward the methanol oxidation reaction, *J. Mater. Chem. A*, 2017, **5**(36), 19467–19475, available from: **https://pubs.rsc.org/en/content/articlehtml/2017/ta/c7ta05102f**.

74 J. Y. Lu, Y. S. Yu, T. B. Chen, C. F. Chang, S. Tamulevičius, D. Erts, *et al.*, Fabrication of an Extremely Cheap Poly(3,4-ethylenedioxythiophene) Modified Pencil Lead Electrode for Effective Hydroquinone Sensing, *Polymers*, 2021, **13**(3), 343, available from: **https://www.mdpi.com/2073-4360/13/3/343/htm**.

75 R. Baronia, J. Goel, J. Kaswan, A. Shukla, S. K. Singhal and S. P. Singh, PtCo/rGO nano-anode catalyst: enhanced power density with reduced methanol crossover in direct methanol fuel cell, *Mater. Renew. Sustain. Energy*, 2018, **7**(4), 1–13, available from: **https://link.springer.com/article/10.1007/s40243-018-0134-8**.

76 N. Bhuvanendran, S. Ravichandran, W. Zhang, Q. Ma, Q. Xu, L. Khotseng, *et al.*, Highly efficient methanol oxidation on durable PtxIr/MWCNT catalysts for direct methanol fuel cell applications, *Int. J. Hydrogen Energy*, 2020, **45**(11), 6447–6460.

77 E. Cossar, M. S. E. Houache, Z. Zhang and E. A. Baranova, Comparison of electrochemical active surface area methods for various nickel nanostructures, *J. Electroanal. Chem.*, 2020, **870**, 114246.

78 E. Lust, Zero Charge Potentials and Electrical Double Layer at Solid Electrodes, in *Encyclopedia of Interfacial Chemistry*, Elsevier, 2018, pp. 316–344.

79 Z. Xie, P. He, L. Du, F. Dong, K. Dai and T. Zhang, Comparison of four nickel-based electrodes for hydrogen evolution reaction, *Electrochim. Acta*, 2013, **88**, 390–394.

80 L. Guan, L. Yu and G. Z. Chen, Capacitive and non-capacitive faradaic charge storage, *Electrochim. Acta*, 2016, **206**, 464–478.

81 F. Karkeh-Abadi, M. Ghiyasiyan-Arani, S. Mustafa Hameed, F. H. Alsultany, H. Hussain Hamza, A. M. Aljeboree, *et al.*, Electrochemical hydrogen storage capabilities of Li2Co2(MoO4)2 nanostructures: Schiff base-assisted synthesis and characterization, *Int. J. Hydrogen Energy*, 2025, **128**, 377–385.

82 R. Martínez-Hincapié, J. Wegner, M. U. Anwar, A. Raza-Khan, S. Franzka, S. Kleszczynski, *et al.*, The determination of the electrochemically active surface area and its effects on the electrocatalytic properties of structured nickel electrodes produced by additive manufacturing, *Electrochim. Acta*, 2024, **476**, 143663.

83 R. Jin, Q. Lu, J. Liao, Y. Zhu, T. Huang, W. Wang, *et al.*, Prompt template-free synthesis of porous PtPb sponge-like nanostructure for electro-oxidation of methanol and carbon monoxide, *Electrochim. Acta*, 2024, **508**, 145210.

84 Q. Lu, R. Jin, T. Huang, Y. Zhu, H. Sun, Z. Su, *et al.*, Facile one-step synthesis of porous PtPb neural network-like nanowires for electrooxidation of methanol with a CO-poisoning tolerance, *Int. J. Hydrogen Energy*, 2024, **91**, 1127–1135.

85 F. Karimi, M. Akin, R. Bayat, M. Bekmezci, R. Darabi, E. Aghapour, *et al.*, Application of Quasihexagonal Pt@PdS2-MWCNT catalyst with High Electrochemical Performance for Electro-Oxidation of Methanol, 2-Propanol, and Glycerol Alcohols For Fuel Cells, *Mol. Catal.*, 2023, **536**, 112874.

86 X. Cao, N. Wang, Y. Han, C. Gao, Y. Xu, M. Li, *et al.*, PtAg bimetallic nanowires: Facile synthesis and their use as excellent electrocatalysts toward low-cost fuel cells, *Nano Energy*, 2015, **12**, 105–114.

87 D. L. Quan and P. H. Le, Enhanced Methanol Oxidation Activity of PtRu/C100−xMWCNTsx (x = 0–100 wt.%) by Controlling the Composition of C-MWCNTs Support, *Coatings*, 2021, **11**(5), 571.

88 R. Baronia, J. Goel, S. Tiwari, P. Singh, D. Singh, S. P. Singh, *et al.*, Efficient electro-oxidation of methanol using PtCo nanocatalysts supported reduced graphene oxide matrix as anode for DMFC, *Int. J. Hydrogen Energy*, 2017, **42**(15), 10238–10247.